



High performance ozone decomposition spinel (Mn,Co)₃O₄ catalyst accelerating the rate-determining step

Le Zhang^{a,b,1}, Jiawei Yang^{c,1}, Anqi Wang^{a,b}, Shaohua Chai^{a,b}, Jian Guan^{a,b}, Linfeng Nie^{a,b}, Guijun Fan^{a,b}, Ning Han^{a,b,d,*}, Yunfa Chen^{a,b,d,**}

^a Key Laboratory of Science & Technology on Particle Materials, Institute of Process Engineering, Chinese Academy of Sciences, Beijing 100190, China

^b School of Chemical Engineering, University of Chinese Academy of Sciences, Beijing 100049, China

^c The Future Lab, Tsinghua University, Beijing 100084, China

^d State Key Laboratory of Multiphase Complex Systems, Institute of Process Engineering, Chinese Academy of Sciences, Beijing 100190, China

ARTICLE INFO

Keywords:

Ozone catalyst
Spinel
Water resistance
In-situ Raman spectroscopy

ABSTRACT

At present, it is still a challenge to develop ozone decomposition catalysts with high efficiency and high humidity resistance. Herein, a series of spinel (Mn,Co)₃O₄ catalysts are synthesized by coprecipitation method. Compared with the Mn₃O₄ and Co₃O₄ analogues, the obtained (Mn,Co)₃O₄ has $Co^{II\cdot}_{Co^{III}}$ acceptor-defect and $Mn^{III\cdot}_{Mn^{II}}$ donor-defect, which could contribute to the electron transfer between catalyst and ozone, accelerating ozone decomposition. Importantly, the in-situ Raman spectra of Mn₃O₄ shows the accumulation of peroxide species (O₂²⁻) inferring that the decomposition of O₂²⁻ is the rate-determining step. On the other side, the reaction of the atomic oxygen with ozone would be rate-determining for Co₃O₄, as revealed by the low efficiency but no O₂²⁻ signal. However, the synergy of Mn and Co in (Mn,Co)₃O₄ accelerates both the rate-determining steps obtaining high efficiency, which provides a new idea to develop catalysts in ozone elimination.

1. Introduction

Although the atmospheric ozone can protect living organisms by absorbing harmful ultraviolet radiation, it is a pollutant near the ground. Ozone not only directly harms living organisms, but also is one of the main causes of photochemical smog pollution [1,2]. Ozone is used widely in the treatment of polluted water, contaminated gas purification, and food sterilization [3,4] because its antiviral, anti-bacteriological, and oxidation properties. However, the concentration of residual ozone from off-gas is high and beyond the admissible level. Therefore, it is necessary to remove the residual ozone, as the release of ozone can cause severe environmental pollution. In addition to industrial ozone emissions, indoor ozone formed by laser printers, photocopiers, and air purifiers also needs to be decomposed, because the concentration of ozone above 0.1 mg m⁻³ is extremely harmful to human health and plants growth [5]. The half-life of ozone decomposition at low temperature is long (half-life of ozone is 160 h at 25 °C in

atmosphere) due to the resonance stabilized structure of ozone [6]. Consequently, it is technologically important to eliminate ozone in environment due to its toxicity and stability.

Generally, the common methods to eliminate ozone include thermal decomposition, catalytic decomposition and liquid adsorption [7]. The catalytic decomposition of ozone has been a research focus because of its unique advantages such as high efficiency, safety, stability, economy, mild reaction conditions and environmental friendliness [7]. Noble metal catalysts (Ag [8], Pt [9] and Au [10]) can be used for effective decomposition of ozone, but high price limits the widely applications. As a result of the relatively high efficiency and low cost, transition metal oxides are studied as ozone catalysts widely. Ma et al. found that Ce-OMS-2 with abundant Mn³⁺ was a promising ozone decomposition catalyst [11]. Gopi et al. found that H-δ-MnO₂ had lower average oxidation of Mn and more surface oxygen vacancies, showed higher ozone decomposition performance than K-δ-MnO₂ [12]. However, it is still a challenge for catalysts to remove ozone under high humidity

* Corresponding author at: Key Laboratory of Science & Technology on Particle Materials, Institute of Process Engineering, Chinese Academy of Sciences, Beijing 100190, China

** Correspondence to: Post: P.O. Box 353, Beijing 100190, China.

E-mail addresses: nhan@ipe.ac.cn (N. Han), chenyf@ipe.ac.cn (Y. Chen).

¹ These authors contributed equally to this work.

condition because the presence of water molecules significantly reduces the ozone elimination efficiency. For instance, ozone decomposition efficiency of MnO_2 decreased from 100% to 90% and 60% with the relative humidity (RH) increase from 10% to 50% and 90%. After cutting off water vapor, the ozone decomposition efficiency was restored to around 100% [13]. Ozone elimination efficiency of amorphous mesoporous MnO_x decrease from 100% to 80% and 55% when the RH increased from 10% to 50% and 70%, respectively [14]. Consequently, it is essential to develop catalytic materials with high humidity resistance and high activity at room temperature.

Spinel-type oxides (a formula as AB_2O_4) have a composition of A-O tetrahedrons and B-O octahedrons, and the adjacent cation can contribute to the catalytic activity by electron exchange [15]. Co_3O_4 is a typical cubic spinel structure oxide with tetrahedrally coordination Co^{2+} sites and octahedrally coordination Co^{3+} sites [16]. And, Mn_3O_4 has a special distorted spinel structure, in which Mn^{2+} are in tetrahedral sites whereas Mn^{3+} are in octahedral sites. Mn_3O_4 with degenerate electronic state would be unstable, undergoing Jahn-Teller distortion along c-axis and modifies to tetragonal $I4_1/amd$ [17]. Spinel has been used as catalysts widely because of their benefits such as controllable valence, morphology, structure and composition [18]. Spinel CoMn_2O_4 showed the temperature with 80% conversion efficiency (T_{80}) of toluene at 320 °C, which exhibited higher catalytic activity than other Mn-based catalysts [19]. Dong et al. reported the spinel CoMn_2O_4 catalyst with rich cationic defects and large specific surface area exhibited high activity for toluene oxidation [20].

In this work, a series of $(\text{Mn},\text{Co})_3\text{O}_4$ spinel catalysts with abundant oxygen vacancy and large special surface area are successful synthesized by the oxalic coprecipitation method and applied for ozone catalytic elimination. The results show that spinel $(\text{Mn},\text{Co})_3\text{O}_4$ exhibits ~100% ozone catalytic performance and stability in harsh condition (300 ppm ozone, 1200,000 $\text{mL g}^{-1} \text{h}^{-1}$, 25 °C) far higher than Mn_3O_4 and Co_3O_4 . With RH increases to 90%, $(\text{Mn},\text{Co})_3\text{O}_4$ maintains high ozone catalytic decomposition efficiency of about 95% while Co_3O_4 and Mn_3O_4 decrease to 24.3% and 69.9%, respectively. The structure of spinel $(\text{Mn},\text{Co})_3\text{O}_4$ is investigated in detail by Raman spectrum, X-ray diffraction (XRD), and extended X-ray absorption fine structure (EXAFS). The results of crystal structure and valence state inferring that $\text{Co}^{II\text{X}}_{\text{Co}^{III}}$ acceptor-defect and $\text{Mn}^{III\text{X}}_{\text{Mn}^{II}}$ donor-defect co-exist in spinel $(\text{Mn},\text{Co})_3\text{O}_4$, contributing to the performance of ozone decomposition. In addition, the mechanism of ozone decomposition on Co_3O_4 is investigated by in-situ Raman spectroscopy, showing that the rate-determining step of ozone catalytic decomposition is the reaction of the atomic oxygen with ozone molecule, different from that of Mn_3O_4 . For spinel $(\text{Mn},\text{Co})_3\text{O}_4$, the synergy of Mn and Co accelerates the rate-determining steps, which contributes to the high efficiency and high humidity resistance.

2. Experimental

2.1. Preparation of samples

The spinel samples were prepared by an oxalic coprecipitation method. Analytical grade Manganese (II) Acetate Dihydrate $((\text{CH}_3\text{COO})_2\text{Mn} \cdot 2 \text{H}_2\text{O})$, Cobalt (II) Acetate Tetrahydrate $((\text{CH}_3\text{COO})_2\text{Co} \cdot 4 \text{H}_2\text{O})$ and oxalic acid were used as raw materials. Typically, a series of $(\text{Mn},\text{Co})_3\text{O}_4$ were synthesized by molar ratios of $(\text{CH}_3\text{COO})_2\text{Mn} \cdot 2 \text{H}_2\text{O}$ and $(\text{CH}_3\text{COO})_2\text{Co} \cdot 4 \text{H}_2\text{O}$ at 1:5, 1:2, 2:1, 5:1, and denoted as M1C5, M1C2, M2C1, M5C1, respectively. Different stoichiometric amount of $(\text{CH}_3\text{COO})_2\text{Mn} \cdot 2 \text{H}_2\text{O}$ and $(\text{CH}_3\text{COO})_2\text{Co} \cdot 4 \text{H}_2\text{O}$ were mixed and dissolved in 20 mL deionized water under magnetic stirring at 80 °C to obtain a homogeneous solution. Then, 20 mL 10 wt% oxalic acid as precipitant was added to the solution and stirred at 80 °C for 20 min. Then the precipitates were centrifuged and washed with deionized water and ethanol three times. The as-obtained products were dried at 80 °C for 12 h and then calcined in a muffle furnace at a ramp of

2 °C min^{-1} from room temperature to 400 °C for 3 h. Unitary Mn_3O_4 and Co_3O_4 were synthesized using the same method by adding merely $(\text{CH}_3\text{COO})_2\text{Mn} \cdot 2 \text{H}_2\text{O}$ and $(\text{CH}_3\text{COO})_2\text{Co} \cdot 4 \text{H}_2\text{O}$.

2.2. Characterizations and catalytic activity evaluation

The morphologies of samples were characterized by scanning electron microscope (SEM) and transmission electron microscope (TEM). The element contents were tested by inductively coupled plasma optical emission spectrometer (ICP-OES). The crystal structure was characterized by XRD, Raman spectra, and EXAFS. The specific surface areas and pore size distributions were characterized by Brunauer-Emmett-Teller (BET) and Barrett-Joyner-Halenda (BJH) methods. The surface atom state and electronic structure were characterized by XPS, electron paramagnetic resonance (EPR), X-ray absorption near edge structure (XANES), and ultraviolet photoelectron spectrometer (UPS). The NH_3 -, H_2O - and O_2 -temperature programmed desorption (TPD) and H_2 -temperature programmed reduction (TPR) experiments were carried out. The details of above characterizations described in Text S1.1.

The adsorbed intermediate species during ozone catalytic decomposition were detected by in-situ Raman spectra (Renishaw Invia Qontor Confocal Raman Microscope, $\lambda = 532 \text{ nm}$). The in-situ Raman spectra were acquired under 100 mL min^{-1} flow with 300 ppm dry or humid ozone.

The ozone catalytic decomposition efficiency was evaluated by 50 mg samples and calculated by equation: $100\% \times (\text{C}_{\text{in}} - \text{C}_{\text{out}})/\text{C}_{\text{in}}$. In addition, the details of catalytic performance test were shown in Text S1.2.

3. Results and discussion

3.1. Ozone catalytic activity

As shown in Fig. 1a, the ozone elimination efficiency of a series of $(\text{Mn},\text{Co})_3\text{O}_4$, Mn_3O_4 , and Co_3O_4 are evaluated in dry ozone flow (300 ppm ozone, 1200,000 $\text{mL g}^{-1} \text{h}^{-1}$, 25 °C). It is shown that a series of $(\text{Mn},\text{Co})_3\text{O}_4$ spinel catalysts (M1C2 (97.3%), M2C1 (97.2%), M1C5 (95.1%), and M5C1 (92.0%)) show higher decomposition efficiency than Co_3O_4 (79.9%) and Mn_3O_4 (78.9%) during 10 h continuous test. And at lower SV of 240,000, all samples show high ozone catalytic activity in dry condition of > 90% as shown in Fig. S1. Some reported catalysts are shown in Table S1, which would be deactivated by water molecules. Therefore, the highly-efficient samples (M1C2, M2C1 and M1C5) were tested under humid ozone atmosphere (300 ppm, 240,000 $\text{mL g}^{-1} \text{h}^{-1}$, RH ~90%) to explore the resistance to humidity, with Mn_3O_4 and Co_3O_4 as comparison. As shown in Fig. 1b, though the ozone catalytic activity will be affected by water vapor, the $(\text{Mn},\text{Co})_3\text{O}_4$ spinel catalysts still show higher efficiency of M2C1 (95.7%), M1C2 (93.3%) and M5C1 (91.7%) than Mn_3O_4 (69.9%) and Co_3O_4 (24.3%) in 10 h continuous test. Therefore, compared with pure Mn_3O_4 and pure Co_3O_4 , $(\text{Mn},\text{Co})_3\text{O}_4$ spinel catalysts (M2C1, M1C2 and M5C1) exhibit higher moisture resistance.

The catalysts were tested further under more harsh environment with gas flow of 1 L min^{-1} at 25 °C (SV = 2400 $\text{L g}^{-1} \text{h}^{-1}$). Because the surface area of M2C1 is higher than the other two, the M2C1 was tested with higher concentration of ozone (900 ppm) while Mn_3O_4 and Co_3O_4 were still tested with 300 ppm ozone. The amount of ozone catalytic decomposition per unit area is calculated by $R = \text{CXF}/(22.4\text{WS})$. The ozone catalytic decomposition efficiency over various catalysts and calculated R is present in Fig. S2 and Table S2, respectively. As shown in Fig. S2, the catalytic efficiency of M2C1 is still higher than the other two in 8 h even the concentration of ozone is 3 times. In addition, as shown in Table S2, the M2C1 (268.37 $\text{mol m}^{-2} \text{h}^{-1}$) exhibit higher the amount of ozone catalytic decomposition per unit area than Co_3O_4 (253.19 $\text{mol m}^{-2} \text{h}^{-1}$) and Mn_3O_4 (165.65 $\text{mol m}^{-2} \text{h}^{-1}$).

In addition, the intrinsic activity was evaluated by the activation

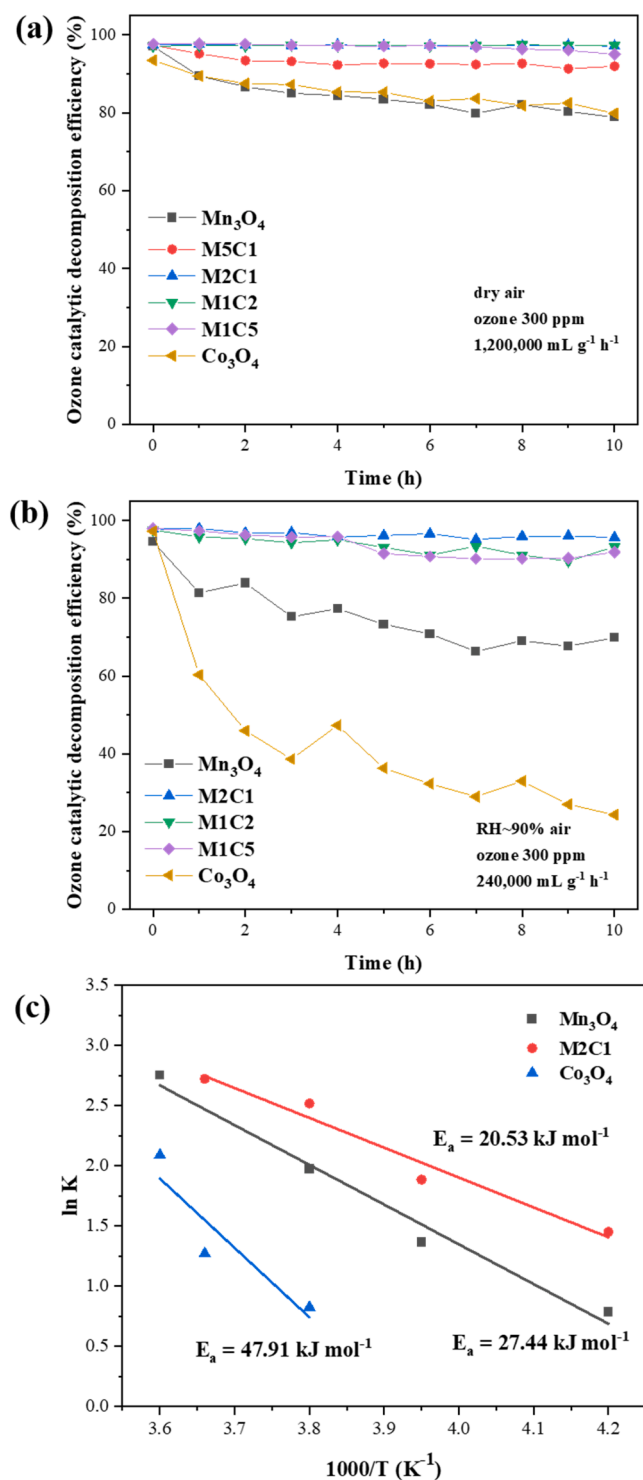


Fig. 1. Ozone catalytic decomposition efficiency as a function of reaction time over Mn₃O₄, (Mn,Co)₃O₄ and Co₃O₄ at ozone inlet concentration: 300 ppm, T = 25 °C, dry air (SV = 1200,000 mL g⁻¹ h⁻¹) (a) and air with RH~90% (SV = 240,000 mL g⁻¹ h⁻¹) (b); Arrhenius plots of the reaction rate constants (activation energies, E_a) on Mn₃O₄, M2C1, and Co₃O₄ (test condition: 25 mg catalysts mixed with 475 mg quartz sand, 300 ppm ozone, total gas flow 1000 mL min⁻¹, temperature from 238 K to 283 K) (c).

energy. The 25 mg samples mixed with 475 mg quartz sand are tested at different temperatures from 238 K to 283 K with 300 ppm ozone and total flow of 1000 mL min⁻¹. The linear plots of Arrhenius results reveal that the ozone decomposition only remains in the kinetically controlled

region at a conversion of less than 20%. On the basis of the slopes of the Arrhenius plots, the apparent activation energies (E_a) have been calculated and shown in Fig. 1c. The M2C1 with lowest E_a (20.53 kJ mol⁻¹) shows the highest ozone catalytic decomposition performance, indicating the intrinsic activity of M2C1 is the higher than the Mn₃O₄ (27.44 kJ mol⁻¹) and Co₃O₄ (47.91 kJ mol⁻¹). Commercial Mn₃O₄ (CAS: 1308-06-1; AR) and commercial Co₃O₄ (CAS: 1317-35-7; 97%) were brought from Macklin. The ozone catalytic decomposition efficiency of the commercial Mn₃O₄ and Co₃O₄ is shown in Fig. S3(a) and the XRD patterns of above them are shown in Fig. S3(b) and. The XRD results show commercial Mn₃O₄ and Co₃O₄ with high crystalline, indicating there are little defects in them and thus lead to low performance.

In summary, the M2C1 not only present comparable ozone removal performance to that of Mn₃O₄ and Co₃O₄ in dry air but also show desirable catalytic activity in a gas flow with water. In order to concisely explore the relationship between high efficiency ozone decomposition and the attribution of spinel materials, the M2C1 is selected as a representative sample to research the attribution of (Mn,Co)₃O₄ spinel in the following sections.

3.2. Crystal structure and textural properties

N₂ adsorption-desorption isotherms of Mn₃O₄, Co₃O₄ and M2C1 are shown in Fig. S2a-c. All above samples exhibit the type IV isotherms and appearance of H3 hysteresis loops, indicating the mesoporous structures. As the decomposition of oxalate precursor releases a large amount of CO and CO₂ during pyrolysis, all samples show high specific surface areas [20,21] of 52.39, 50.78, 146.21, 136.54, 101.32, and 109.02 m²g⁻¹ for Mn₃O₄, Co₃O₄, M5C1, M2C1, M1C2, and M1C5, respectively (as shown in Table S2). The different ratios of Mn and Co spinel samples show similar high specific surface areas, which are all higher than those of Mn₃O₄ and Co₃O₄. The pore size distribution shows that all above samples have a number of 0–10 nm mesoporous. High surface areas are beneficial to exposing more active sites for ozone catalytic decomposition. Hence, the relatively higher surface area of M2C1 might be one factor contributing to the high ozone catalytic decomposition activity.

Fig. 2a-c show the morphologies of Mn₃O₄, Co₃O₄ and M2C1 by SEM. The result shows that Mn₃O₄ is coral-like irregular nanoparticles while Co₃O₄ and M2C1 are slit-like polygon nanoparticles. The slit-like meso-pores are formed by rapid heating of oxalate precursor releasing steam and carbon oxides violently. The results of TEM of Mn₃O₄, Co₃O₄ and M2C1 are shown in Fig. 2d-f, and insets are the HRTEM images. The lattice fringe space over Mn₃O₄ is 0.31 nm which is corresponding to the (112) facet. For Co₃O₄, the lattice fringe spaces are 0.48 and 0.28 nm which are in agreement with the (111) and (220) facets respectively. The lattice fringe space of M2C1 is 0.49 nm which is corresponding to the (101) facet of spinel CoMn₂O₄ phase (JCPDS: 00-001-1126).

The crystallographic structure of samples, measured by XRD, are shown in Fig. 3a. The result shows that Co₃O₄ has the cubic spinel-type phase (JCPDS: 00-001-1152) and Mn₃O₄ has the tetragonal hausmannite phase (JCPDS: 00-008-0017). As for M2C1, all peaks shift to lower 2θ values and become broadened obviously compared with those of Co₃O₄, as the radii of Mn cations are larger than those of Co cations. According to XRD patterns of different ratios of Mn and Co samples (Fig. S5), it is obvious that all samples show spinel structure. With the proportion of Mn in spinel increases the M1C5, M1C2, and M2C1 still show cubic spinel-type Co₃O₄ phase. The peak locations of above three samples shift to lower 2θ because the radii of Mn cations are larger than those of Co cations. In addition, the more Mn in samples, the more shift in XRD. As for M5C1, it shows special distorted spinel-type Mn₃O₄ phase. In summary, the XRD pattern results show that though the contents of Mn and Co are much different, the M1C5, M1C2, and M2C1 exhibit similar crystallographic structure. The poor crystallinity of samples which are caused by the nanoscale crystallites, makes the XRD

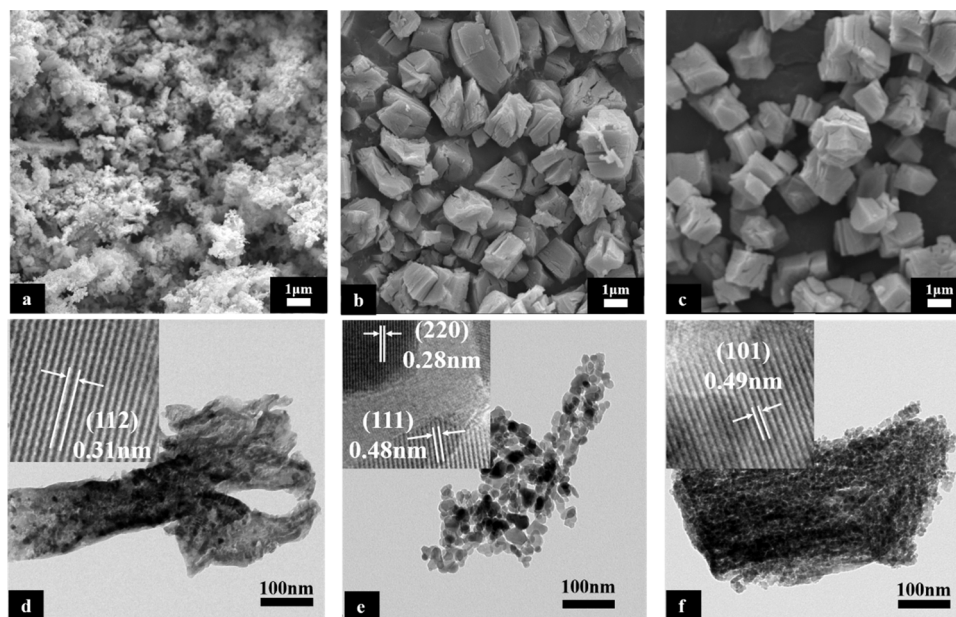


Fig. 2. SEM images of Mn_3O_4 (a), Co_3O_4 (b) and M2C1 (c), TEM images of Mn_3O_4 (d), Co_3O_4 (e) and M2C1 (f) (insets are HRTEM images).

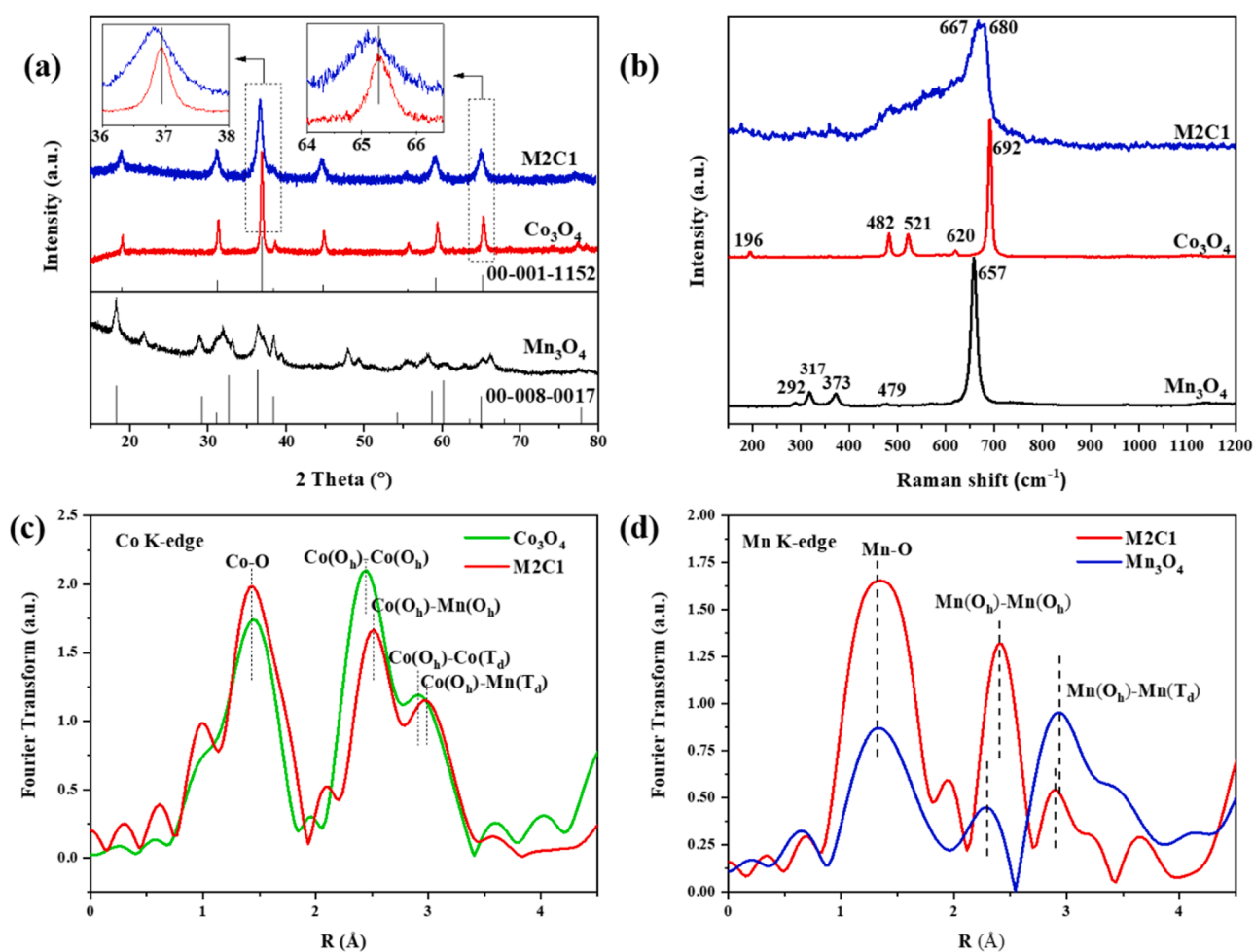


Fig. 3. XRD pattern (a), Raman spectra (b), R-space of Co EXAFS spectra of M2C1 and Co_3O_4 (c), and Mn EXAFS spectra of M2C1 and Mn_3O_4 (d) of as-prepared catalysts.

characterization a real challenge. In order to overcome these difficulties, Raman spectroscopy, a sensitive to short-range metal-oxygen arrangements spectroscopic technique, has been used to characterize these materials. Spinel type oxides exhibit five Raman-allowed lattice modes as predicted by group theory [22]. As shown in Fig. 3b the Raman spectrum of Mn_3O_4 shows clearly a main band at 657 cm^{-1} , which is attributed to the Mn-O breathing vibration of Mn^{2+} in the Mn_3O_4 tetrahedral coordination. It is attributed to the A_1g mode of vibration. The two weak bands at 317 and 373 cm^{-1} are also assigned to Mn_3O_4 tetrahedral coordination, which are assigned to T_2g mode of vibration [23]. In addition, the two minor peaks located at 292 and 479 cm^{-1} are also the same as previous literature [22,24]. For the Co_3O_4 , the Raman bands located at 196 , 482 , 521 , 620 , and 692 cm^{-1} have $F_{1/2g}$, E_g , $F_{2/2g}$, $F_{3/2g}$, and A_1g symmetry, respectively. In addition, the band at 692 and 196 cm^{-1} are assigned to the characteristics of octahedral sites (CoO_6) and tetrahedral sites (CoO_4), respectively [25–27]. Hence, the bands at 196 and 692 cm^{-1} are assigned to Raman vibration of $\text{Co}(\text{Td})\text{-O}$ and $\text{Co}(\text{Oh})\text{-O}$, respectively. For the M2C1, both the peak location and intensity have changed a lot, which indicates that the original coordinative environment of site octahedral and tetrahedral site are changed. The changes in Raman spectrum is due to the polyhedral distortion of spinel lattice and change of bond lengths of cation-anion after Co substituting Mn partly. There are tetrahedral sites of (MnO_4) and (CoO_4) and octahedral sites of (MnO_6) and (CoO_6) in spinel M2C1. One strong band at 667 cm^{-1} in M2C1 has a 10 cm^{-1} blue-shift comparing with 657 cm^{-1} in Mn_3O_4 , due to substitution of tetrahedral sites Mn by Co. The other strong band at 680 cm^{-1} in M2C1 has a 12 cm^{-1} red-shift comparing with 692 cm^{-1} in Co_3O_4 , due to substitution of octahedral sites Co by Mn. Curve fitting of Raman spectra for M2C1 has been made as shown in Fig. S6. According to above Raman spectrum analyses, it can be sure that the structure of all catalysts is spinel, and the lattice of M2C1 is distorted due to Co and Mn mixing.

The coordination environments of Mn_3O_4 , Co_3O_4 and M2C1 are further confirmed by EXAFS spectra as shown in Fig. 3c and d. The radial distances are apparent distance without phase correction, so a typical value of $0.3\text{--}0.4\text{ \AA}$ must be added to apparent distance to convert to real bond distance [25]. One peak below 2 \AA corresponds to first Metal-Oxygen shell and the attribution of other peaks below 4 \AA depends on the metal coordination environment. If the metal cation is tetrahedrally (Td) coordinated by 1.3 oxygen anion (coordination number (CN) 4), there is only one type of distance from this cation to its neighboring metal cation noted as $\text{M}(\text{Td})\text{-M}(\text{Oh})$. Nevertheless, if the metal cation is octahedrally (Oh) coordinated by 4 oxygen (CN 8), there are two types of distance from this neighboring metal cation: $\text{M}(\text{Oh})\text{-M}(\text{Oh})$ and $\text{M}(\text{Oh})\text{-M}(\text{Td})$ [27]. As shown in Fig. 3c, there are three main peaks below 4 \AA in Co EXAFS spectra of Co_3O_4 . The first band below 2 \AA relates to the Co-O shells, including tetrahedral coordination $\text{Co}(\text{Td})\text{-O}$ and octahedral coordination $\text{Co}(\text{Oh})\text{-O}$, and the second and third peaks correspond to $\text{Co}(\text{Oh})\text{-Co}(\text{Oh})$ and $\text{Co}(\text{Oh})\text{-Co}(\text{Td})$. In the Co EXAFS spectrum of M2C1, the first main peak is similar to that of Co_3O_4 , suggesting that the first Co-O has not changed. However, the second and third peaks shift to larger distance obviously, confirming that Co has been substituted by Mn with larger radii leading to $\text{Co}(\text{Oh})\text{-Mn}(\text{Oh})$ and $\text{Co}(\text{Oh})\text{-Mn}(\text{Td})$. Both the Mn EXAFS spectra of Mn_3O_4 and M2C1 show three main peaks below 4 \AA in Fig. 3d. For Mn_3O_4 , three peaks are attributed to $\text{Mn}(\text{Oh})\text{-O}/\text{Mn}(\text{Td})\text{-O}$, $\text{Mn}(\text{Oh})\text{-Mn}(\text{Oh})$, and $\text{Mn}(\text{Oh})\text{-Mn}(\text{Td})$, respectively [28]. Compared with Mn_3O_4 , the first peak location of M2C1 is similar, suggesting that Mn-O distance is not changed. Nevertheless, the third peak, which is assigned to the distance of $\text{Mn}(\text{Oh})\text{-Co}(\text{Td})$, shifts towards a shorter distance being assigned to the replacement of Mn by Co cation with smaller radii. However, due to the distortion of the spinel lattice, the second peak shifts to a larger distance, resulting in an increase in the distance of $\text{Mn}(\text{Oh})\text{-Mn}(\text{Oh})$. According to above EXAFS results, it is confirmed that all samples are spinel structure and M2C1 has four Metal-Oxygen coordination types: MnO_4 , MnO_6 , CoO_4 and CoO_6 , which are consistent with the result of XRD and Raman

spectra.

3.3. Surface atom state and electronic structure

Ozone catalytic decomposition is a typical heterogeneous reaction occurring at solid-gas interface and thus catalytic activity is closely related to the surface chemical states. Therefore, XPS is used to investigate the state of Mn, Co and O. Species with d^4 , d^9 in octahedral coordination and high spin d^7 , d^5 , d^2 and low spin d^4 in tetrahedral coordination are susceptible to distortion. Distortion of the Mn^{3+}O_6 octahedra lowers the symmetry because the Mn cation has four unpaired electrons in 'd' orbital [17]. Therefore, as for the cation valence state of spinel Mn_3O_4 , there are two kinds of formula: $\text{Mn}^{2+}\text{Mn}_2^{3+}\text{O}_4$ and $\text{Mn}^{4+}\text{Mn}_2^{2+}\text{O}_4$ which contain bivalent, trivalent and quadrivalent Manganese cations. As shown in Fig. 4a, the manganese species of Mn_3O_4 and M2C1 located at 643 ± 0.2 , 641.8 ± 0.2 , and $640.6 \pm 0.2\text{ eV}$ can be attributed to Mn^{4+} , Mn^{3+} , and Mn^{2+} , respectively [29,30]. The exact locations of the peaks are shown in Table S5. The contents of each Mn species are shown in Table 1, suggesting the average Mn state of M2C1 (3.59) is higher than that of Mn_3O_4 (3.55). As shown in Co 2p spectra (Fig. 4b) of Co_3O_4 , the major Co $2p_{3/2}$ peaks could be deconvoluted into Co^{2+} ($\sim 780.4\text{ eV}$) and Co^{3+} ($\sim 779.3\text{ eV}$) [31,32]. In addition, there are three satellite peaks located at ~ 786 , ~ 790 and $\sim 804\text{ eV}$ [33]. The exact locations of the peaks are also shown in Table S5. The average valence state of Co for Co_3O_4 is 2.36, which is much lower than theoretical valence state (2.67), indicating that abundant surface oxygen vacancies are generated to maintain the electrostatic balance [26]. Compared with Co_3O_4 , the Co $2p_{3/2}$ and $2p_{1/2}$ binding energy of M2C1 locate at 780.4 and 795.5 eV , which are attributed to Co^{2+} [33]. The result is consistent with literature reporting that the valence state of Co cation in Co-poor M2C1 spinel is normally $+2$ [33,34]. The presence of Mn in M2C1 could lead to the reduction of Co by an internal redox reaction [34,35]. Hence, the Mn valence state of M2C1 is higher than Mn_3O_4 , which could be assigned to the oxidation of Mn by internal redox reaction. As shown in Fig. 4c and d, XANES at the K-edge of Co and Mn are used to study the valence states of Co and Mn in Mn_3O_4 , Co_3O_4 and M2C1, respectively. Fig. 4c suggests that the Mn cation valence state in M2C1 is higher than Mn_3O_4 and Fig. 4d indicates the valence state of Co_3O_4 is higher than M2C1, which are consistent with XPS results. According to above analysis of surface atom state and crystal structure, for M2C1, there are both CoO_4 and CoO_6 coordination in the Co^{2+} valence state. Therefore, Co^{2+} partly replaces Co^{3+} in CoO_6 and forms $\text{Co}_{\text{CoO}_6}^{\text{IIx}}$ acceptor-defect. In addition, compared with Mn_3O_4 , the content of Mn^{3+} in M2C1 gets higher but of Mn^{2+} gets lower, inferring partly Mn^{3+} replaces Mn^{2+} and forms $\text{Mn}_{\text{Mn}}^{\text{IIIx}}$ donor-defect. As shown in Fig. S7(a) and S7(b), the XPS spectra of Mn 2p and Co 2p of other samples (M5C1, M1C2, M1C5) results show the intensity of peaks increase with the content of Mn or Co while the locations of peaks are the same, indicating the surface states of Mn or Co are similar though the contents are different.

There are three kinds of peaks in the O 1s spectra (Fig. 4e), which are located around at 534 , 531 and 529.8 eV and attributed to chemisorbed oxygen (O_c), surface oxygen vacancy (O_v) and surface lattice oxygen (O_l) [20], respectively. The concentrations of O_v are evaluated by the peak areas and exhibited in Table 1. The O_v content of M2C1 (37.4%) is higher than those of Mn_3O_4 (35.2%) and Co_3O_4 (34.9%) and the ratio of O_v/O_l shows the same result. According to previous literatures, oxygen molecules preferentially adsorb at the catalyst surface oxygen vacancies [36,37]. Consequently, spinel M2C1 with high O_v concentration can provide sufficient active sites for ozone adsorption and catalytic decomposition. In addition, owing to the unsaturated coordination of the surface atoms, there are a large number of defects on the surface, which provide abundant oxygen vacancies [13,37]. Abundant oxygen vacancies are beneficial to electron transfer, which are critical for ozone decomposition. Therefore, the M2C1 with more oxygen vacancies shows

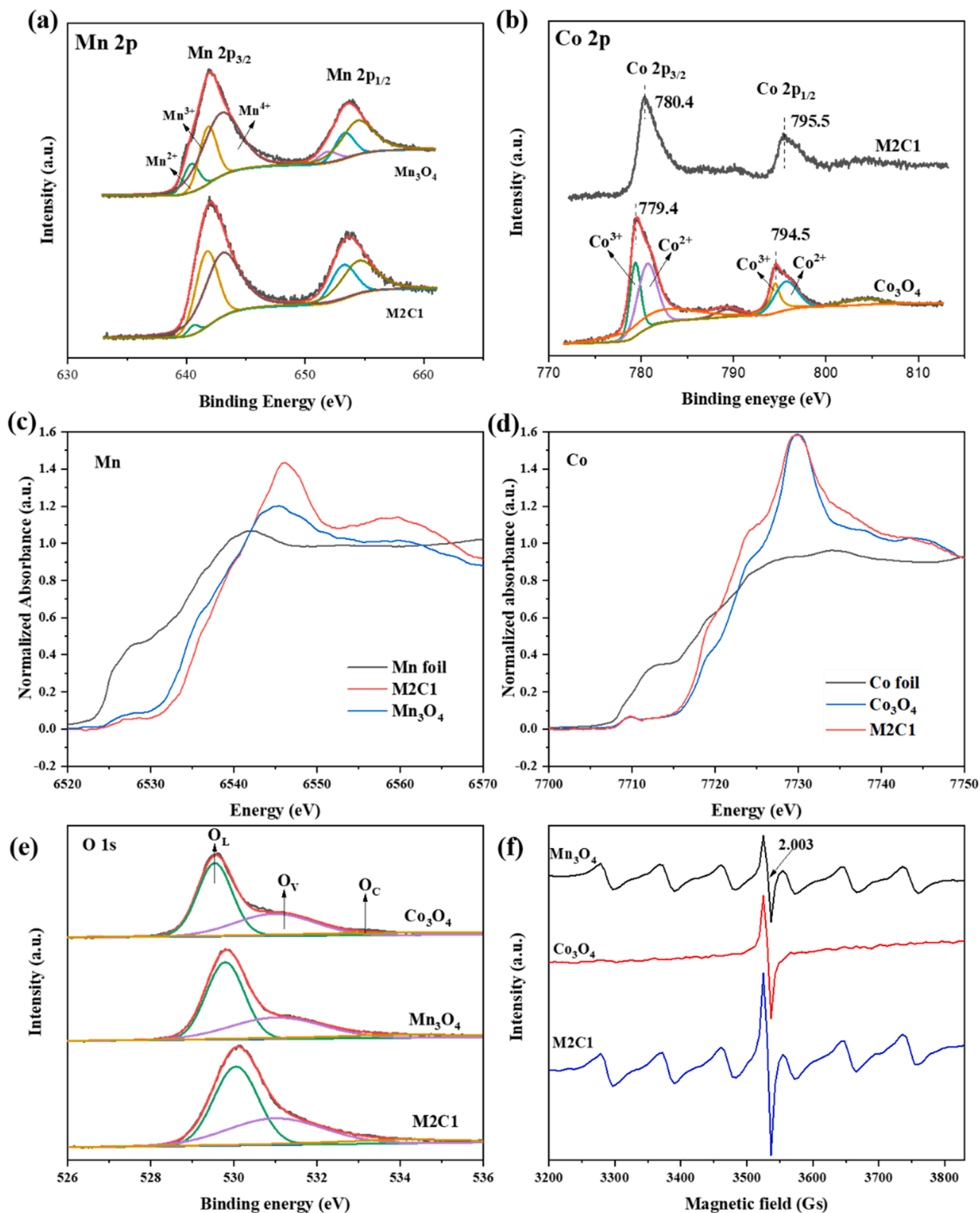


Fig. 4. XPS spectra of Mn 2p (a), Co 2p (b) and O 1s (e), normalized XANES spectra at the Mn K-edge of Mn₃O₄ and M2C1 (c), normalized XANES spectra at the Co K-edge of Co₃O₄ and M2C1 (d), and EPR spectra (f) of as-prepared catalysts.

higher performance in ozone decomposition.

EPR is used to identify the oxygen vacancies of Mn₃O₄, Co₃O₄ and M2C1 in this work. As shown in Fig. 4f, there are seven signals in Mn₃O₄ and M2C1 while there is only one signal in Co₃O₄. The signal at $g = 2.003$, which appears in the EPR spectroscopy of all above samples,

is attributed to the electrons trapped on the oxygen vacancies [38]. The higher intensity of signal means the more oxygen vacancies. Therefore, the order of oxygen vacancy concentration goes from high to low is M2C1, Co₃O₄ and Mn₃O₄, which is consistent with XPS of O 1s spectra and O₂-TPD results. In addition, there are six-line resonance in Mn₃O₄

Table 1
Surface composition and oxidation state of catalysts.

Catalysts	Mn ²⁺ (%)	Mn ³⁺ (%)	Mn ⁴⁺ (%)	O _L (%)	O _V (%)	O _A (%)	O _V / O _L
Mn ₃ O ₄	10.7	23.7	65.6	52.2	35.2	12.5	67.4
M2C1	2.2	36.4	61.4	51.5	37.4	11.1	72.7
Co ₃ O ₄				52.8	34.9	12.3	66.2

and M2C1, which arises from Mn²⁺ (*S*=5/2) and is characteristic of hyperfine interactions (nuclear spin *I* = 5/2) [39]. The clear resolution of this six-line signal suggests the appearance of Mn²⁺ in tetrahedral coordination (MnO₄) in both Mn₃O₄ and M2C1, which is in agreement with Raman and EXAFS results.

Seiichiro found that the conductance of p-type semiconductors would increase after introducing ozone because decomposition of ozone abstracted electrons from the catalysts and made the level of acceptor increase [8]. The work function is defined as the minimum energy required to transfer an electron from a point within a solid to a point just outside its surface. Therefore, the lower work function is benefit for ozone abstracting electrons from sample surface during ozone catalytic decomposition and thus catalysts with lower work function shows better ozone elimination performance. UPS spectra, shown in Fig. 5, is used to study the work function of Mn₃O₄, Co₃O₄, and M2C1, which is calculated by equation: $\Phi = h\nu - E_{\text{cutoff}} + E_{\text{Fermi}}$. The E_{cutoff} of Mn₃O₄, Co₃O₄, and M2C1 locate at 5.48, 6.87, and 7.36 eV, respectively, while the E_{Fermi} of above samples are both at -6.88 eV. Hence, the work functions of Mn₃O₄, Co₃O₄, and M2C1 are 8.86, 7.47, and 6.98 eV, respectively. Compared with Mn₃O₄ and Co₃O₄, the M2C1 shows lower work function and thus it is easier for ozone to abstract electrons during ozone catalytic decomposition, showing better ozone elimination efficiency.

3.4. TPD and TPR studies

Ozone can be adsorbed and dissociated on the surface Lewis acid sites of catalysts because of its basic property, leading to forming atomic oxygen [37]. Hence, high acidity of catalyst is benefit of ozone decomposition. As shown in Fig. 6a, the acidity is characterized by NH₃-TPD. The M2C1 exhibits strong NH₃ desorption peaks for surface acid sites at the intermediate temperature, while Co₃O₄ and Mn₃O₄ display weak peaks. Li et al. reported previously that at low temperature the main desorption originated from residual physical adsorbed NH₄⁺ and/or NH₃ species bonded to hydroxyl surface groups weakly, while the desorption at medium temperature is derived from the coordination of

NH₃ with Lewis acid site [40]. The global acidity is shown in Table 2, which is calculated by the amount of desorbed NH₃. It shows that Mn₃O₄ and Co₃O₄ exhibit similarly low global acidity, which are 0.478 mmol g⁻¹ and 0.487 mmol g⁻¹, respectively. The M2C1 displays more acidic surface sites, 0.594 mmol g⁻¹, which would adsorb and react with ozone, attributing to the higher activity and humidity resistance than Co₃O₄ and Mn₃O₄.

H₂O-TPD profiles are further performed to assess the humidity resistance. The moisture resistance of the catalysts increases with the decrease of water desorption temperature [40]. The peaks are originated from adsorbed H₂O molecules contacted with the samples surface directly (type A H₂O), structural hydroxyl group clusters (type B H₂O), and strongly bonded hydroxyl groups (type C H₂O) at < 250 °C, 250–400 °C, and > 400 °C respectively [41,42]. As shown in Fig. 6b, M2C1 illustrates four peaks at 200, 330, 480, and 780 °C, while Co₃O₄ shows three peaks at 280, 450, and 680 °C and Mn₃O₄ shows only one peak at 630 °C. Therefore, it can be apparently shown that M2C1 is easier to desorb H₂O molecules (i.e. low adsorbility) and thus has better moisture resistance.

As shown in Fig. 6c, the reducibility of catalysts is evaluated by H₂-TPR. For Mn₃O₄, there are three reduction peaks at 355, 429 and 509 °C, being assigned to the reduction of Mn⁴⁺ to Mn³⁺, Mn³⁺ to Mn²⁺ and Mn²⁺ to Mn⁰ [43]. As for Co₃O₄, there are two peaks at 385 and 498 °C, which are attributed to the reduction of Co³⁺ to Co²⁺ and Co²⁺ to Co⁰, respectively [21,44]. There are three peaks at 316, 436, and 734 °C for M2C1. The peaks at 316 and 436 °C are assigned to reduction of Mn⁴⁺ to Mn³⁺, Mn³⁺ to Mn²⁺, and Co³⁺ to Co²⁺. In addition, the board peak at 734 °C is ascribed to the reduction of Co²⁺ to Co⁰ and Mn²⁺ to Mn⁰. Combined with XPS analysis, M2C1 has much more oxygen vacancies compared with Co₃O₄ and Mn₃O₄. In addition, the reduction peaks of M2C1 shift to lower temperatures, which could be assigned to the O_V [21], as the presence of O_V could loosen the bond strength and thus the M-O bonds in M2C1 could be broken more easily, leading to higher reducibility. The higher reducibility and weaker M-O band could help the O₂²⁻ adsorption and desorption during the ozone decomposition [40, 44].

O₂-TPD profiles are assessed to evaluate the oxygen desorption performances as shown in Fig. 6d. The peaks are classified into four parts: desorption of physically adsorbed oxygen below 200 °C, desorption of chemisorbed oxygen on oxygen vacancy at 200–400 °C, desorption of near-surface lattice oxygen at 400–600 °C and desorption of bulk lattice oxygen above 600 °C [26]. Compared with Co₃O₄ and Mn₃O₄, M2C1 can desorb more oxygen at low temperature of 200–400 °C, which is good consistent with XPS results. The relatively easier oxygen desorption of M2C1 would contribute to the higher ozone decomposition activity as chemisorbed oxygen is the key intermediate (O₂²⁻) in ozone decomposition [45], which is then investigated in detail.

3.5. Ozone decomposition mechanism

Oyama et al. proposed that the ozone decomposition on supported manganese oxide involved three sequence steps, which were consisted of dissociative adsorption of ozone to form an oxygen molecule and an atomic oxygen species (step 1), reaction of the atomic species with gaseous ozone molecule to form an adsorbed O₂²⁻ and gas phase oxygen (step 2), and decomposition of the O₂²⁻ and desorption of molecular oxygen (step 3) [46]. The reaction process could be clarified clearly by Eqs. (1–3).



where the symbol * represents catalysts surface reaction sites. The first reaction is fast, while the following two reactions are relatively slower,

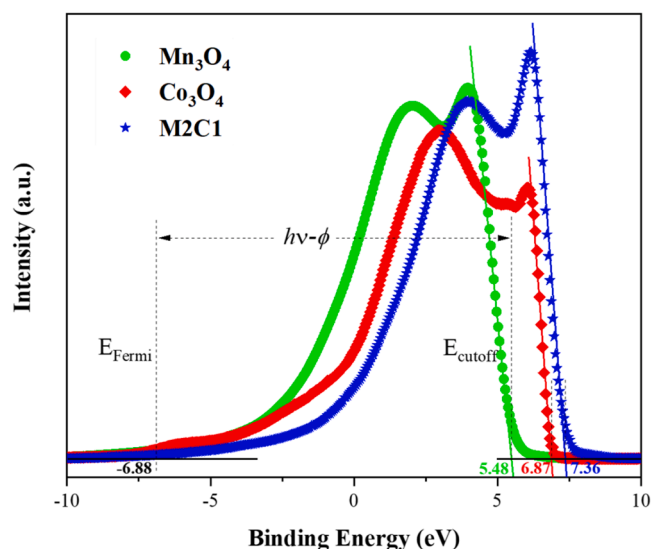


Fig. 5. UPS spectra of Mn₃O₄, Co₃O₄, and M2C1.

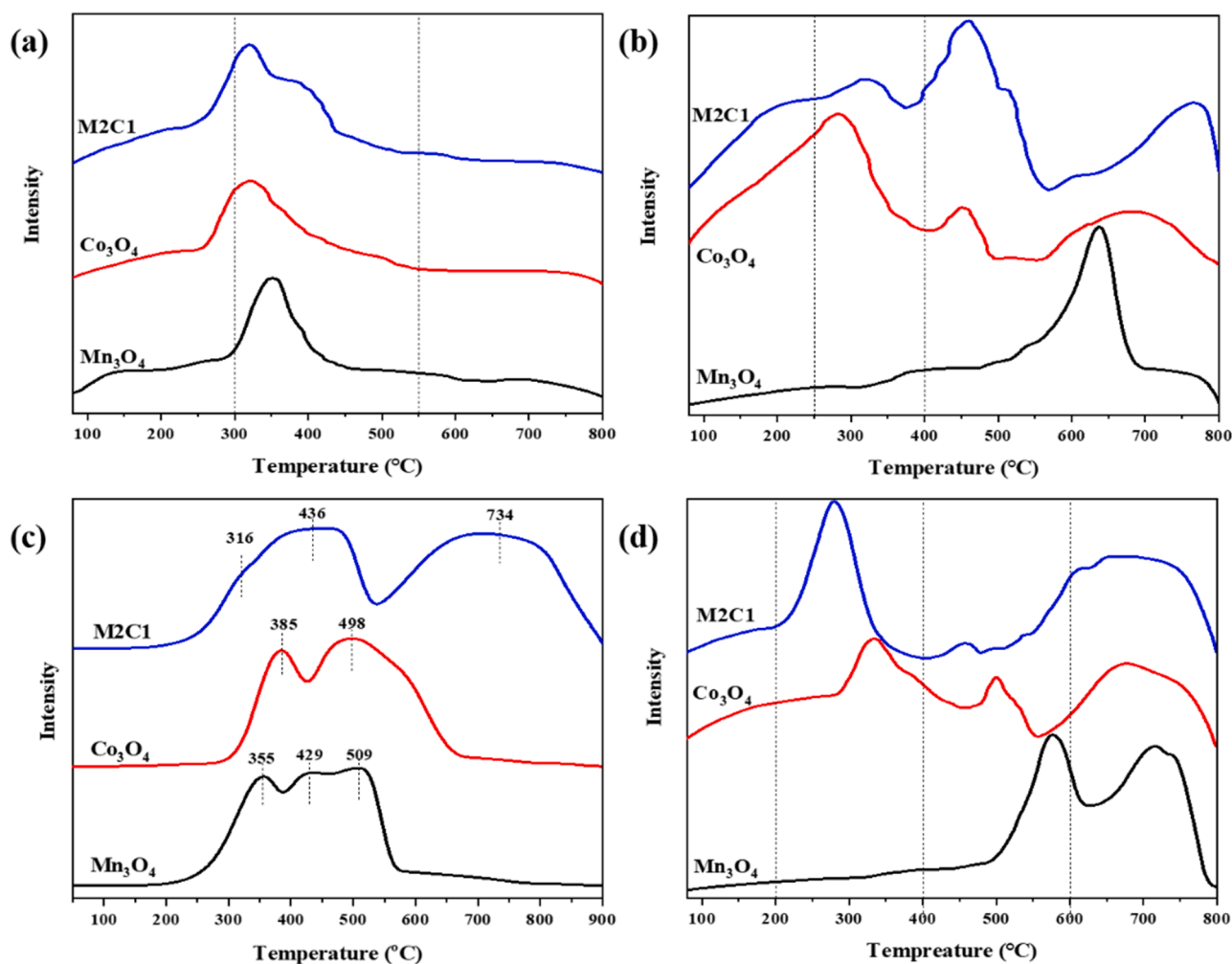


Fig. 6. NH_3 -TPD (a), H_2O -TPD (b), H_2 -TPR (c), and O_2 -TPD (d) profiles of prepared samples.

Table 2

The amounts of NH_3 desorbed estimated by integration of the area under the NH_3 -TPD curve.

Catalysts	Mn_3O_4	Co_3O_4	M2C1
Quantity (mmol NH_3/g)	0.478	0.487	0.594

which determine the coverage of O_2^{2-} , and step 3 is the slowest becoming the rate-determining step [6,46].

In-situ Raman spectroscopy is applied to study adsorbed intermediates during ozone decomposition, as shown in Fig. 7. For Mn_3O_4 (Fig. 7a), as soon as introducing ozone whether there is water vapor or not, there will be a new Raman signal at 875 cm^{-1} , which can be attributed to the adsorbed O_2^{2-} [46,47]. In addition, the intensity increases after introducing water vapor, indicating that the presence of water molecules will reduce the O_2^{2-} desorption speed which leads to more accumulated O_2^{2-} than in dry flow. Consequently, water molecules competitively adsorb with ozone molecules and more O_2^{2-} accumulation results in the decline of ozone conversion on Mn_3O_4 in humid flow. In addition, the peak will disappear after cutting off ozone due to desorption of the O_2^{2-} , indicating that the O_2^{2-} is intermediate of ozone catalytic decomposition. The presence of O_2^{2-} indicates that the desorption of O_2^{2-} is slow, serving as the rate-determining step during ozone catalytic decomposition on the surface of Mn_3O_4 [46,47].

As for Co_3O_4 (Fig. 7b), no new signal appears in in-situ Raman spectra after introducing dry ozone flow, indicating that there is no

accumulation of O_2^{2-} on the surface of Co_3O_4 . However, as the ozone decomposition efficiency reduces gradually as shown in Fig. 1, there would be another rate-determining step on Co_3O_4 rather than the step 3 on Mn_3O_4 . It is noted that when the catalyst is brought into ozone flow, its surface is quickly covered by atomic oxygen species through dissociative adsorption of ozone on the acidic sites (Eq. 1). And Co_3O_4 shows similar acidity to Mn_3O_4 according to the result of NH_3 -TPD in Fig. 5 and Table 2, indicating the step 1 on Co_3O_4 would be as quick as that on Mn_3O_4 . Therefore, the rate-determining step of ozone decomposition on Co_3O_4 surface is the too slow formation speed of O_2^{2-} in step 2. After introducing water vapor, the ozone decomposition efficiency of Co_3O_4 reduces obviously, indicating that water molecules competitive adsorption would reduce the catalytic activity of Co_3O_4 . However, there is still no new Raman signal appearing even though there are water molecules, indicating that competitive adsorption of water molecule with ozone on Co_3O_4 , unlike on Mn_3O_4 , will not lead to the accumulation of O_2^{2-} . Therefore, the result in humid flow further verifies the hypothesis that the step 2 is the rate-determining step of ozone decomposition on Co_3O_4 .

For M2C1, there is no new Raman signal appearing in dry ozone flow as shown in Fig. 7c, indicating that there is no accumulation of O_2^{2-} on the surface of M2C1 similar to that of Co_3O_4 . However, as M2C1 keeps high ozone decomposition efficiency as shown in Fig. 1, both step 2 and step 3 are quick because of the synergy of Mn and Co in spinel M2C1. After introducing water vapor, there is a weak signal appearing in in-situ Raman spectra, indicating that the water molecules competitively adsorb with ozone leading to the accumulation of O_2^{2-} . Moreover, the

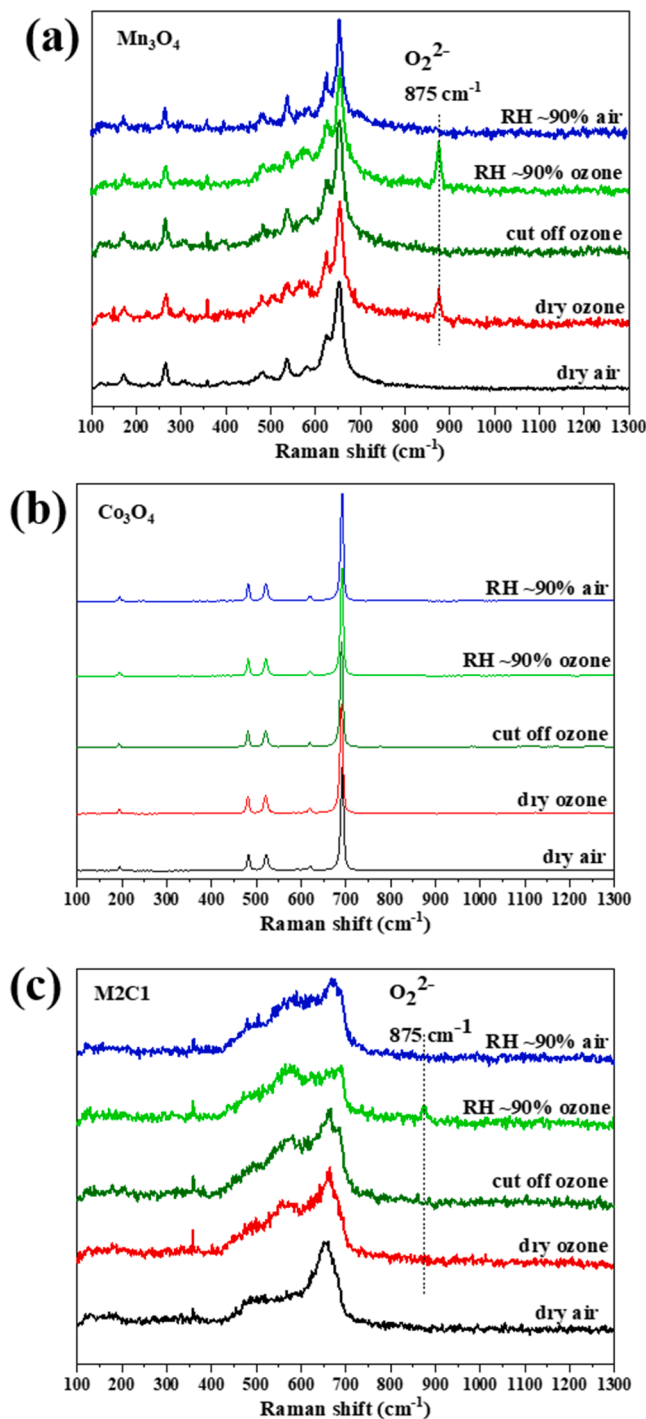


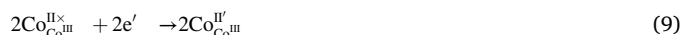
Fig. 7. In-situ Raman spectra of Mn_3O_4 (a), Co_3O_4 (b) and M2C1 (c) under air and ozone flow in dry and humid conditions.

same location of the weak peak at 875 cm^{-1} as in Mn_3O_4 spectra indicates that the signal is attributed to O_2^{2-} on Mn rather than Co in M2C1. Therefore, step 2 would be fast on Mn sites and step 3 would be fast on Co sites (i.e., synergy of Mn and Co) which enables the high ozone catalytic decomposition efficiency of M2C1. Even though water molecules would occupy partly Co sites in moist flow, which makes the accumulation of O_2^{2-} on Mn sites, the ozone catalytic decomposition still keep high efficiency on M2C1.

To further clarify the mechanism differences of Mn_3O_4 , Co_3O_4 , and M2C1, the schematic illustrations of ozone decomposition reaction are shown in Fig. 8. The mechanism of ozone decomposition on Mn_3O_4 is in

good agreement with previous reports, which consist of three steps and the rate-determining step is step 3. The ozone elimination efficiency reduces a lot in humid ozone flow because of competitive adsorption of water molecules and more accumulated O_2^{2-} . However, as for Co_3O_4 , there is no new signal appeared in in-situ Raman spectra no matter in dry flow or humid flow, indicating that the rate-determining step of ozone catalytic decomposition is step 2. There is also no new signal in in-situ Raman spectra on M2C1 in dry ozone flow and the ozone catalytic decomposition efficiency keeps high and stable, indicating no accumulation of O_2^{2-} . This is attributed to the synergy of Mn and Co, and steps 2 and 3 of ozone catalytic decomposition on M2C1 surface are much quicker than those on Co_3O_4 and Mn_3O_4 . In addition, corresponding reaction mechanism diagram in $(\text{Mn},\text{Co})_3\text{O}_4$ under humid condition has been made in Fig. S8(a), and the decomposition mechanism over Co_3O_4 and Mn_3O_4 are also shown in Fig. S8(b) for comparison. For Co_3O_4 and Mn_3O_4 (Fig. S8(b)), oxygen vacancies would be occupied by water molecules and thus the efficiency of ozone decomposition decreases. By contrast, $\text{Co}_{\text{Co}^{III}}^{\text{II}\times}$ acceptor-defect sites in the $(\text{Mn},\text{Co})_3\text{O}_4$ share some water molecules adsorption with oxygen vacancies make it have enough activity sites for high ozone catalytic decomposition under humid condition (Fig. S8(a)).

According to above analysis of crystal structure and surface atom state, there are Co^{2+} lying in tetrahedral and octahedral coordinated sites, inferring that the Co^{2+} partly replaces the Co^{3+} in octahedral coordinated sites and form $\text{Co}_{\text{Co}^{III}}^{\text{II}\times}$ acceptor-defect. Similarly, the Mn^{4+} partly replaces the Mn^{3+} and forms $\text{Mn}_{\text{Mn}^{III}}^{\text{IV}\times}$ donor-defect. The $\text{Mn}_{\text{Mn}^{III}}^{\text{IV}\times}$ would contribute free electrons in M2C1 as shown in Eq. (5), while the first two steps of ozone decomposition, shown in Eqs. (6) and (7), need electrons and form O^- and O_2^{2-} . In addition, as shown in Eq. 4, the oxygen vacancy could release an electron which could be grasped by ozone and form the ion-sorbed oxygen O_2^{2-} [48]. Owing to the contribution of free electrons from $\text{Mn}_{\text{Mn}^{III}}^{\text{IV}\times}$ donor-defect in M2C1, the first two steps, especially the second step, would be quicker than Mn_3O_4 . Nevertheless, in the third step, O_2^{2-} would release electron and desorb from active site to form O_2 (Eq. (8)). The $\text{Co}_{\text{Co}^{III}}^{\text{II}\times}$ would deplete electrons, as shown in Eq. (9), contributing to the electrons transfer from O_2^{2-} back to the M2C1 surface and the formation of O_2 . Hence, the third step of ozone decomposition on M2C1 will be quicker than Co_3O_4 . Consequently, the co-exist of $\text{Co}_{\text{Co}^{III}}^{\text{II}\times}$ and $\text{Mn}_{\text{Mn}^{III}}^{\text{IV}\times}$ in M2C1 will accelerate both the step 2 and 3, showing far higher ozone elimination efficiency than the Mn_3O_4 and Co_3O_4 analogues.



4. Conclusion

A series of spinel $(\text{Mn},\text{Co})_3\text{O}_4$ are synthesized by oxalic coprecipitation method and adopted for ozone catalytic decomposition. All spinel $(\text{Mn},\text{Co})_3\text{O}_4$ show far higher efficiency of $> 90\%$ than the Mn_3O_4 and Co_3O_4 analogues in harsh environments of 300 ppm ozone, $240,000\text{ cm}^3\text{g}^{-1}\text{h}^{-1}$ space velocity and 90% RH. The high activity is attributable to the high surface area, co-existed $\text{Mn}_{\text{Mn}^{III}}^{\text{IV}\times}$ donor-defect and $\text{Co}_{\text{Co}^{III}}^{\text{II}\times}$ acceptor-defect, abundant oxygen vacancy, high acidity and low oxygen and H_2O adsorbility. Importantly, the in-situ Raman spectra

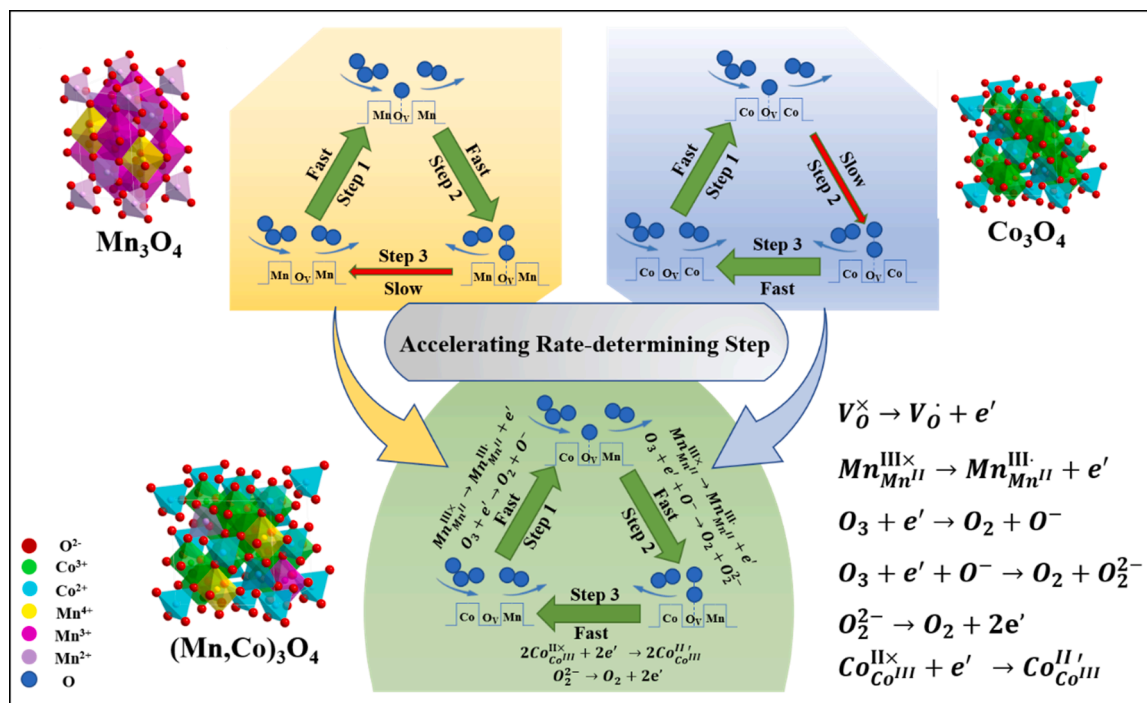


Fig. 8. Schematic representations and ozone decomposition illustration of Mn_3O_4 , Co_3O_4 and $(\text{Mn},\text{Co})_3\text{O}_4$.

shows that the rate-determining steps of Mn_3O_4 and Co_3O_4 are the desorption of intermediate peroxide species (O_2^{2-}) and the reaction of the atomic oxygen with ozone to form the O_2^{2-} . However, the synergy of Mn and Co in spinel $(\text{Mn},\text{Co})_3\text{O}_4$ accelerates both the rate-determining steps obtaining high efficiency, which provides a new idea to develop catalysts with high efficiency and high humidity resistance in ozone decomposition reaction.

CRediT authorship contribution statement

Le Zhang: Conceptualization, Data curation, Formal analysis, Investigation, Methodology, Validation, Visualization, Writing – original draft, Writing – review & editing. **Jiawei Yang:** Writing, Conceptualization, Data curation, Formal analysis, Investigation, Methodology, Validation, Visualization, Writing – original draft, Writing – review & editing. **Anqi Wang:** Writing – review & editing. **Shaohua Chai:** Writing – review & editing. **Jian Guan:** Writing – review & editing. **Linfeng Nie:** Writing – review & editing. **GuiJun Fan:** Writing – review & editing. **Ning Han:** Conceptualization, Formal analysis, Funding acquisition, Methodology, Project administration, Writing – review & editing. **Yunfa Chen:** Funding acquisition, Supervision.

Declaration of Competing Interest

The authors declare that they have no known competing financial interests or personal relationships that could have appeared to influence the work reported in this paper.

Acknowledgments

This research was financially supported by the National Key Research and Development Program of China (2016YFC0207100).

Appendix A. Supporting information

Supplementary data associated with this article can be found in the online version at [doi:10.1016/j.apcatb.2021.120927](https://doi.org/10.1016/j.apcatb.2021.120927).

References

- [1] R. Atkinson, Atmospheric chemistry of VOCs and NO_x , Atmos. Environ. 34 (2000) 2063–2101, [https://doi.org/10.1016/S1352-2310\(99\)00460-4](https://doi.org/10.1016/S1352-2310(99)00460-4).
- [2] J.A. Bernstein, N. Alexis, H. Bacchus, I.L. Bernstein, P. Fritz, E. Horner, N. Li, S. Mason, A. Nel, J. Oullette, K. Reijula, T. Reponen, J. Seltzer, A. Smith, S. M. Tarlo, The health effects of nonindustrial indoor air pollution, J. Allergy Clin. Immunol. 121 (2008) 585–591, <https://doi.org/10.1016/j.jaci.2007.10.045>.
- [3] F. Lin, Z. Wang, Q. Ma, Y. Yang, R. Whiddon, Y. Zhu, K. Cen, Catalytic deep oxidation of NO by ozone over MnO_x loaded spherical alumina catalyst, Appl. Catal. B Environ. 198 (2016) 100–111, <https://doi.org/10.1016/j.apcatb.2016.05.058>.
- [4] Z.B. Guzel-Seydim, A.K. Greene, A.C. Seydim, Use of ozone in the food industry, LWT Food Sci. Technol. 37 (2004) 453–460, <https://doi.org/10.1016/j.lwt.2003.10.014>.
- [5] S.D. RAZUMOVSKII, G.E. ZAIKOV, Ozone and its reactions with organic compounds, Stud. Org. Chem. 15 (1984).
- [6] S.T.E.D. OYAMA, Chemical and catalytic properties of ozone, Catal. Rev. 42 (2000) 279–322, <https://doi.org/10.1081/CR-100100263>.
- [7] X. Li, J. Ma, H. He, Recent advances in catalytic decomposition of ozone, J. Environ. Sci. 94 (2020) 14–31, <https://doi.org/10.1016/j.jes.2020.03.058>.
- [8] S. Imamura, M. Ikebata, T. Ito, T. Ogita, Decomposition of ozone on a silver catalyst, Ind. Eng. Chem. Res. 30 (1991) 217–221, <https://doi.org/10.1021/ie00049a033>.
- [9] W.T. Tsai, C.Y. Chang, F.H. Jung, C.Y. Chiu, W.H. Huang, Y.H. Yu, H.T. Liou, Y. Ku, J.N. Chen, C.F. Mao, Catalytic decomposition of ozone in the presence of water vapor, J. Environ. Sci. Heal. Part A 33 (1998) 1705–1717, <https://doi.org/10.1080/10934529809376813>.
- [10] Z. Hao, D. Cheng, Y. Guo, Y. Liang, Supported gold catalysts used for ozone decomposition and simultaneous elimination of ozone and carbon monoxide at ambient temperature, Appl. Catal. B Environ. 33 (2001) 217–222, [https://doi.org/10.1016/S0926-3373\(01\)00172-2](https://doi.org/10.1016/S0926-3373(01)00172-2).
- [11] J. Ma, C. Wang, H. He, Transition metal doped cryptomelane-type manganese oxide catalysts for ozone decomposition, Appl. Catal. B Environ. 201 (2017) 503–510, <https://doi.org/10.1016/j.apcatb.2016.08.050>.
- [12] T. Gopi, G. Swetha, S. Chandra Shekar, C. Ramakrishna, B. Saini, R. Krishna, P.V. L. Rao, Catalytic decomposition of ozone on nanostructured potassium and proton containing $\delta\text{-MnO}_2$ catalysts, Catal. Commun. 92 (2017) 51–55, <https://doi.org/10.1016/j.catcom.2017.01.002>.
- [13] Y. Yu, S. Liu, J. Ji, H. Huang, Amorphous MnO_2 surviving calcination: an efficient catalyst for ozone decomposition, Catal. Sci. Technol. 9 (2019) 5090–5099, <https://doi.org/10.1039/c9cy01426h>.
- [14] S. Liu, J. Ji, Y. Yu, H. Huang, Facile synthesis of amorphous mesoporous manganese oxides for efficient catalytic decomposition of ozone, Catal. Sci. Technol. 8 (2018) 4262–4273, <https://doi.org/10.1039/c8cy01111g>.
- [15] H. Yang, F. Hu, Y. Zhang, L. Shi, Q. Wang, Controlled synthesis of porous spinel cobalt manganese oxides as efficient oxygen reduction reaction electrocatalysts, Nano Res. 9 (2016) 207–213, <https://doi.org/10.1007/s12274-016-0982-4>.

- [16] D. Gu, C.-J. Jia, C. Weidenthaler, H.-J. Bongard, B. Spliethoff, W. Schmidt, F. Schüth, Highly ordered mesoporous cobalt-containing oxides: structure, catalytic properties, and active sites in oxidation of carbon monoxide, *J. Am. Chem. Soc.* 137 (2015) 11407–11418, <https://doi.org/10.1021/jacs.5b06336>.
- [17] A. Moses Ezhil Raj, S.G. Victoria, V.B. Jothy, C. Ravidhas, J. Wollschläger, M. Suendorf, M. Neumann, M. Jayachandran, C. Sanjeeviraja, XRD and XPS characterization of mixed valence Mn_3O_4 hausmannite thin films prepared by chemical spray pyrolysis technique, *Appl. Surf. Sci.* 256 (2010) 2920–2926, <https://doi.org/10.1016/j.apsusc.2009.11.051>.
- [18] Q. Zhao, Z. Yan, C. Chen, J. Chen, Spinel: controlled preparation, oxygen reduction/evolution reaction application, and beyond, *Chem. Rev.* 117 (2017) 10121–10211, <https://doi.org/10.1021/acs.chemrev.7b00051>.
- [19] S.A. Hosseini, D. Salari, A. Niaei, F. Deganello, G. Pantaleo, P. Hojati, Chemical-physical properties of spinel CoMn_2O_4 nano-powders and catalytic activity in the 2-propanol and toluene combustion: effect of the preparation method, *J. Environ. Sci. Heal. Part A* 46 (2011) 291–297, <https://doi.org/10.1080/10934529.2011.539093>.
- [20] C. Dong, Z. Qu, Y. Qin, Q. Fu, H. Sun, X. Duan, Revealing the highly catalytic performance of spinel CoMn_2O_4 for toluene oxidation: involvement and replenishment of oxygen species using in situ designed-TP techniques, *ACS Catal.* 9 (2019) 6698–6710, <https://doi.org/10.1021/acscatal.9b01324>.
- [21] Y. Feng, L. Li, S. Niu, Y. Qu, Q. Zhang, Y. Li, W. Zhao, H. Li, J. Shi, Controlled synthesis of highly active mesoporous Co_3O_4 polycrystals for low temperature CO oxidation, *Appl. Catal. B Environ.* 111–112 (2012) 461–466, <https://doi.org/10.1016/j.apcatb.2011.10.035>.
- [22] H.D. Lutz, B. Müller, H.J. Steiner, Lattice vibration spectra. LIX. Single crystal infrared and Raman studies of spinel type oxides, *J. Solid State Chem.* 90 (1991) 54–60, [https://doi.org/10.1016/0022-4596\(91\)90171-D](https://doi.org/10.1016/0022-4596(91)90171-D).
- [23] B.J. Rani, M. Ravina, G. Ravi, S. Ravichandran, V. Ganesh, R. Yuvakkumar, Synthesis and characterization of hausmannite (Mn_3O_4) nanostructures, *Surf. Interfaces* 11 (2018) 28–36, <https://doi.org/10.1016/j.surfin.2018.02.007>.
- [24] S. Bernardini, F. Bellatreccia, A. Casanova Muncicchia, G. Della Ventura, A. Sodo, Raman spectra of natural manganese oxides, *J. Raman Spectrosc.* 50 (2019) 873–888, <https://doi.org/10.1002/jrs.5583>.
- [25] X. Wang, Y. Liu, T. Zhang, Y. Luo, Z. Lan, K. Zhang, J. Zuo, L. Jiang, R. Wang, Geometrical-site-dependent catalytic activity of ordered mesoporous Co-based spinel for benzene oxidation: in situ drifts study coupled with Raman and XAFS spectroscopy, *ACS Catal.* 7 (2017) 1626–1636, <https://doi.org/10.1021/acscatal.6b03547>.
- [26] Y. Jian, M. Tian, C. He, J. Xiong, Z. Jiang, H. Jin, L. Zheng, R. Albilali, J.-W. Shi, Efficient propane low-temperature destruction by Co_3O_4 crystal facets engineering: Unveiling the decisive role of lattice and oxygen defects and surface acid-base pairs, *Appl. Catal. B Environ.* 283 (2021), 119657, <https://doi.org/10.1016/j.apcatb.2020.119657>.
- [27] Y. Lou, J. Ma, X. Cao, L. Wang, Q. Dai, Z. Zhao, Y. Cai, W. Zhan, Y. Guo, P. Hu, G. Lu, Y. Guo, Promoting Effects of In_2O_3 on Co_3O_4 for CO Oxidation: tuning O_2 activation and CO adsorption strength simultaneously, *ACS Catal.* 4 (2014) 4143–4152, <https://doi.org/10.1021/cs501049r>.
- [28] J. Rosen, G.S. Hutchings, F. Jiao, Synthesis, structure, and photocatalytic properties of ordered mesoporous metal-doped Co_3O_4 , *J. Catal.* 310 (2014) 2–9, <https://doi.org/10.1016/j.jcat.2013.05.003>.
- [29] Z. Shu, Y. Chen, W. Huang, X. Cui, L. Zhang, H. Chen, G. Zhang, X. Fan, Y. Wang, G. Tao, D. He, J. Shi, Room-temperature catalytic removal of low-concentration NO over mesoporous Fe–Mn binary oxide synthesized using a template-free approach, *Appl. Catal. B Environ.* 140–141 (2013) 42–50, <https://doi.org/10.1016/j.apcatb.2013.03.030>.
- [30] W. Tang, X. Wu, D. Li, Z. Wang, G. Liu, H. Liu, Y. Chen, Oxalate route for promoting activity of manganese oxide catalysts in total VOCs' oxidation: effect of calcination temperature and preparation method, *J. Mater. Chem. A* 2 (2014) 2544–2554, <https://doi.org/10.1039/C3TA13847J>.
- [31] J. Bae, D. Shin, H. Jeong, B.S. Kim, J.W. Han, H. Lee, Highly water-resistant La-doped Co_3O_4 catalyst for Co oxidation, *ACS Catal.* 9 (2019) 10093–10100, <https://doi.org/10.1021/acscatal.9b02920>.
- [32] M. Li, F. Bi, Y. Xu, P. Hao, K. Xiang, Y. Zhang, S. Chen, J. Guo, X. Guo, W. Ding, Effect of residual chlorine on the catalytic performance of Co_3O_4 for CO oxidation, *ACS Catal.* 9 (2019) 11676–11684, <https://doi.org/10.1021/acscatal.9b03797>.
- [33] H. Liu, X. Zhu, M. Li, Q. Tang, G. Sun, W. Yang, Single crystal ($\text{Mn},\text{Co})_3\text{O}_4$ octahedra for highly efficient oxygen reduction reactions, *Electrochim. Acta* 144 (2014) 31–41, <https://doi.org/10.1016/j.electacta.2014.08.087>.
- [34] P.A. Joy, S.K. Date, Unusual magnetic hysteresis behavior of oxide spinel MnCo_2O_4 , *J. Magn. Magn. Mater.* 210 (2000) 31–34, [https://doi.org/10.1016/S0304-8853\(99\)00765-9](https://doi.org/10.1016/S0304-8853(99)00765-9).
- [35] H. Liu, L. Zhang, J. Zhang, D. Ghosh, J. Jung, B.W. Downing, E. Whittemore, Electrocatalytic reduction of O_2 and H_2O_2 by adsorbed cobalt tetramethoxyphenyl porphyrin and its application for fuel cell cathodes, *J. Power Sources* 161 (2006) 743–752, <https://doi.org/10.1016/j.jpowsour.2006.04.132>.
- [36] J. Jia, P. Zhang, L. Chen, Catalytic decomposition of gaseous ozone over manganese dioxides with different crystal structures, *Appl. Catal. B Environ.* 189 (2016) 210–218, <https://doi.org/10.1016/j.apcatb.2016.02.055>.
- [37] K.M. Bulanin, A.V. Alexeev, D.S. Bystrov, J.C. Lavalley, A.A. Tsyganenko, IR study of ozone adsorption on SiO_2 , *J. Phys. Chem.* 98 (1994) 5100–5103, <https://doi.org/10.1021/j100070a026>.
- [38] S. Gong, X. Wu, J. Zhang, N. Han, Y. Chen, Facile solution synthesis of Cu_2O – CuO – $\text{Cu}(\text{OH})_2$ hierarchical nanostructures for effective catalytic ozone decomposition, *CrystEngComm* 20 (2018) 3096–3104, <https://doi.org/10.1039/C8CE00203G>.
- [39] M.M. Najafpour, M. Kompany-Zareh, A. Zahraei, D. Jafarian Sedigh, H. Jaccard, M. Khoshkam, R.D. Britt, W.H. Casey, Mechanism, decomposition pathway and new evidence for self-healing of manganese oxides as efficient water oxidizing catalysts: new insights, *Dalt. Trans.* 42 (2013) 14603–14611, <https://doi.org/10.1039/C3DT51406D>.
- [40] S. Gong, Z. Xie, W. Li, X. Wu, N. Han, Y. Chen, Highly active and humidity resistive perovskite LaFeO_3 based catalysts for efficient ozone decomposition, *Appl. Catal. B Environ.* 241 (2019) 578–587, <https://doi.org/10.1016/j.apcatb.2018.09.041>.
- [41] Q. Dai, L.-L. Yin, S. Bai, W. Wang, X. Wang, X.-Q. Gong, G. Lu, Catalytic total oxidation of 1,2-dichloroethane over VO_x/CeO_2 catalysts: further insights via isotopic tracer techniques, *Appl. Catal. B Environ.* 182 (2016) 598–610, <https://doi.org/10.1016/j.apcatb.2015.10.016>.
- [42] V.M. Gun'ko, V.I. Zarko, B.A. Chuikov, V.V. Dudnik, Y.G. Ptushinskii, E.F. Voronin, E.M. Pakhllov, A.A. Chuiko, Temperature-programmed desorption of water from fumed silica, silica/titania, and silica/alumina, *Int. J. Mass Spectrom. Ion Process.* 172 (1998) 161–179, [https://doi.org/10.1016/S0168-1176\(97\)00269-3](https://doi.org/10.1016/S0168-1176(97)00269-3).
- [43] F. Ji, Y. Men, J. Wang, Y. Sun, Z. Wang, B. Zhao, X. Tao, G. Xu, Promoting diesel soot combustion efficiency by tailoring the shapes and crystal facets of nanoscale Mn_3O_4 , *Appl. Catal. B Environ.* 242 (2019) 227–237, <https://doi.org/10.1016/j.apcatb.2018.09.092>.
- [44] Z. Wang, W. Wang, L. Zhang, D. Jiang, Surface oxygen vacancies on Co_3O_4 mediated catalytic formaldehyde oxidation at room temperature, *Catal. Sci. Technol.* 6 (2016) 3845–3853, <https://doi.org/10.1039/C5CY01709B>.
- [45] B. Dhandapani, S.T. Oyama, Gas phase ozone decomposition catalysts, *Appl. Catal. B Environ.* 11 (1997) 129–166, [https://doi.org/10.1016/S0926-3373\(96\)00044-6](https://doi.org/10.1016/S0926-3373(96)00044-6).
- [46] W. Li, G.V. Gibbs, S.T. Oyama, Mechanism of ozone decomposition on a manganese oxide catalyst. 1. In Situ Raman Spectroscopy and Ab initio molecular orbital calculations, *J. Am. Chem. Soc.* 120 (1998) 9041–9046, <https://doi.org/10.1021/ja981441+>.
- [47] J. Jia, P. Zhang, L. Chen, The effect of morphology of $\alpha\text{-MnO}_2$ on catalytic decomposition of gaseous ozone, *Catal. Sci. Technol.* 6 (2016) 5841–5847, <https://doi.org/10.1039/C6CY00301J>.
- [48] A. Wang, L. Zhang, M.G. Rahimi, S. Gong, L. Nie, N. Han, Y. Chen, Defect engineering of ZnO for electron transfer in O_3 catalytic decomposition, *Appl. Catal. B Environ.* 277 (2020), 119223, <https://doi.org/10.1016/j.apcatb.2020.119223>.